Characterizations of AgInSbTe and Its Nanocomposite Thin Films for Phase-Change Memory Applications

Yu-Jen Huang, Tzu-Chin Chung, Chiung-Hsin Wang, and Tsung-Eong Hsieh[z]

Department of Materials Science and Engineering, National Chiao Tung University, Hsinchu, Taiwan 30010, Republic of China

Phase transition kinetics and microstructures of AgInSbTe (AIST) and AIST-SiO$_2$ nanocomposite applied to phase-change memories (PCMs) are investigated. In situ electrical property measurement found that the incorporation of SiO$_2$ escalates the recrystallization temperature (T_x) of nanocomposite. Both X-ray diffraction and transmission electron microscopy showed grain refinement in the nanocomposite which, in turn, results in an increase of the activation energy (E_a) of phase transition, as indicated by subsequent Kissinger's analysis. Increase of T_x and E_a in the nanocomposite was ascribed to AIST grain refinement and hindrance to grain growth due to dispersed SiO$_2$ particles in the sample matrix. Johnson–Mehl–Avrami analysis revealed the decrease of Avrami exponent in nanocomposite, implying that the dispersed SiO$_2$ particles promote the heterogeneous phase transition. Static *I–V* characteristics and reversible binary switching behavior of PCM devices not only confirmed the results of microstructure characterizations but also illustrated the feasibility of the AIST and its nanocomposite layer for PCM fabrication.
© 2010 The Electrochemical Society. [DOI: 10.1149/1.3502531] All rights reserved.

Phase-change memory (PCM) has been recognized as next-generation nonvolatile memory device due to its advantages, including good scalability, high operation speed, low power consumption, high recording density, signal endurance, etc.[1-9] Instead of using laser beam as the heating source in optical data storage, PCM devices utilize a current pulse to heat the phase-change programming layer embedded in devices for signal recording. In order to reduce operating current of PCM devices, various methods have been proposed. One is to define a smaller programming volume by modifying the PCM cell structure, while the other is to modify the physical properties of phase-change materials by, for instance, increasing the resistivity of the phase-change layer in the crystalline state by doping a small amount of nitrogen (N),[1,2] oxygen (O),[3,4] silicon (Si),[5,6] silicon oxide (SiO$_x$),[7-9] etc.

In contrast to the nucleation-dominated GeSbTe (GST) alloys, binary Sb$_2$Te alloys are termed as the growth-dominated chalcogenides.[10] In practice, Sb$_2$Te alloys are usually doped with desired elements for physical property improvement.[11] The Sb$_2$Te alloys doped with silver (Ag) and indium (In), i.e., the quaternary AgInSbTe (AIST), are known to possess better cycling stability of amorphous phase and higher crystallization sensitivity in comparison with other phase-change materials.[12,13] Further, the study on digital versatile disk containing AIST illustrated that the disk possesses high recording density and data-transfer rate features.[14] Good optical properties imply that AIST might also be a promising material for PCM application. However, the electrical properties of AIST are less reported and a further study to identify its feasibility to PCM is required.

Previous studies reported that incorporating SiO$_2$ in GST may effectively improve the stability of amorphous GST and reduce the reset current of PCM devices.[8,9] Recent studies relating to optical data storage reported that the AIST–SiO$_2$ nanocomposite layer can be easily fabricated by the target-attachment method[15] or using a composite sputtering target,[15] and the presence of SiO$_2$ particles is found to hinder the grain growth of AIST. This implies that the formation of nanocomposite is a viable way to modify the microstructure and hence the phase-change behaviors of AIST. This work performs an electrical study on the AIST–SiO$_2$ nanocomposite layer in order to gain an understanding on its PCM applicability.

In situ electrical property measurement, X-ray diffraction (XRD), and transmission electron microscopy (TEM) are the main tools adopted in this work to study the electrical properties and microstructure changes of AIST as well as AIST–SiO$_2$ nanocomposite layers, so as to explore their phase-change kinetics in terms of the fundamental nucleation and growth theories. Meanwhile, the cross-point-type PCM devices with 160-μm contact hole containing AIST and its nanocomposite layer as the programming layers were prepared, and the current–voltage (*I–V*) characteristics on static mode and binary switching behavior were presented as follows.

Experimental

Quaternary AIST alloy with stoichiometric ratio Ag$_2$In$_7$Sb$_{64}$Te$_{27}$ was adopted for subsequent sample preparation. The pristine AIST and the nanocomposite layer containing 85 wt % AIST and 15 wt% SiO$_2$ (termed 85A15S hereafter) were prepared in accord with the method reported previously.[15] The thin-film samples with various thicknesses were deposited on the thermally oxidized Si wafers by a sputtering system at a background pressure better than 1 $\times$ 10^{-6} Torr. Microstructure changes corresponding to the amorphous-to-crystallization transition of above samples were evaluated by using an in situ heating XRD facility equipped with a Mar 345 image plate detector at (Marresearch GmbH, Germany) Beamline BL01C2 of National Synchrotron Radiation Research Center (NSRRC) at Hsinchu, Taiwan, R.O.C. The specimens were installed in a controlled-ambient chamber filled with purified Ar gas and heated at a rate of 1°C/min. The XRD characterizations were carried out in grazing incident manner with a fixed incident angle = 1°, diffraction angle (2θ) up to 45°, and X-ray wavelength = 0.1033 nm. In the meantime, a JEOL JEM 2100FX TEM (JEOL Ltd., Japan) was adopted to observe the microstructure changes of samples subjected to annealing treatment.

The resistivity (ρ) changes of thin-film samples during heating were recorded by using an in situ electrical property measurement system.[16] Exothermal experiment in conjunction with the Kissinger theory[17] and isothermal experiment in conjunction with Johnson–Mehl–Avrami (JMA) theory[18,19] were separately performed. The data obtained were analyzed to secure the key parameters relating to phase transition, including recrystallization temperature (T_x), activation energy (E_a), Avrami exponent (n), and appropriate activation energy (ΔH).

Cross-point-type devices containing AIST or 85A15S nanocomposite as the programming layers were fabricated in order to evaluate their feasibility for PCM. On the thermal oxidized Si wafer, a 100-nm-thick W/Ti film was first deposited and patterned to form the bottom electrode. A 150-nm-thick SiO$_2$ layer was then deposited by plasma-enhanced chemical vapor deposition (PECVD) process. Afterward, photolithography and reactive ion etching (RIE, SAMCO Inc., Japan, RIE-10NR) processes were carried out to pattern the circular contact holes (i.e., the via hole) with the diameter = 160μm. The 150-nm-thick AIST or 85A15S nanocomposite layer and 100-nm-thick W/Ti top electrode layers were se-
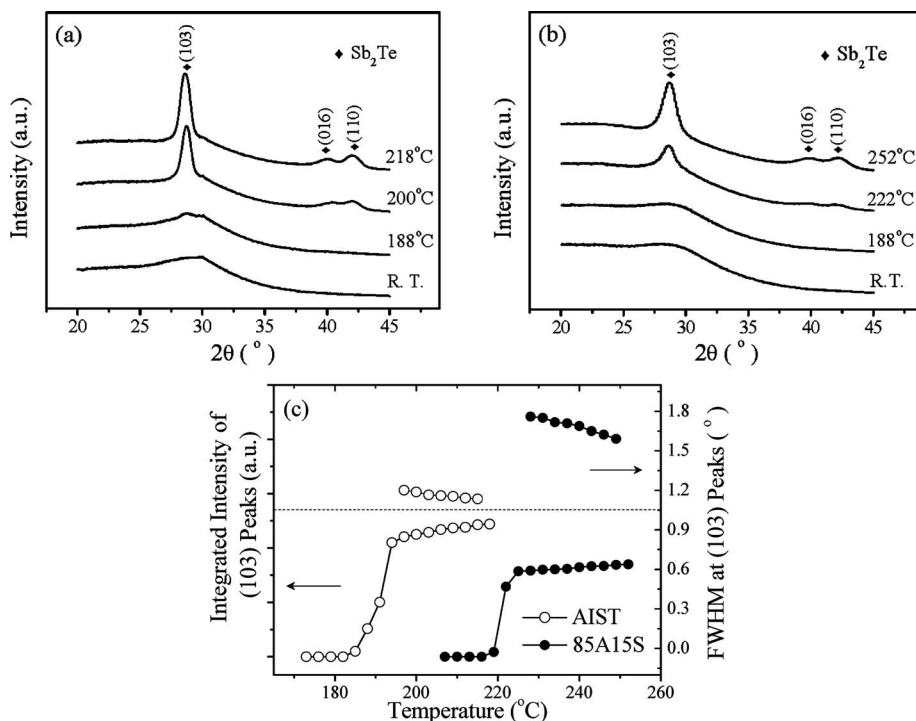
^{z} E-mail: tehsieh@mail.nctu.edu.tw
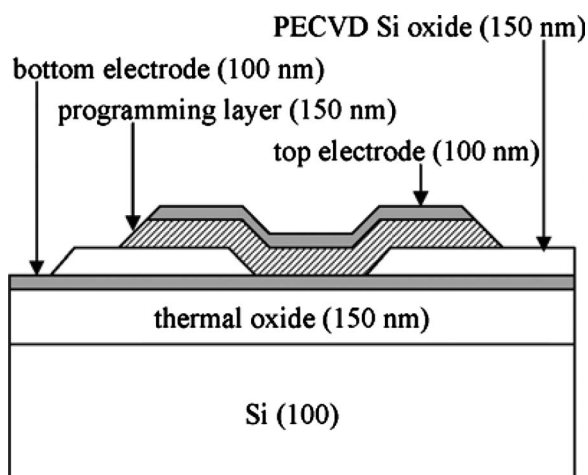
Figure 1. Cross-sectional view and dimensions of PCM device fabricated for static *I–V* test.
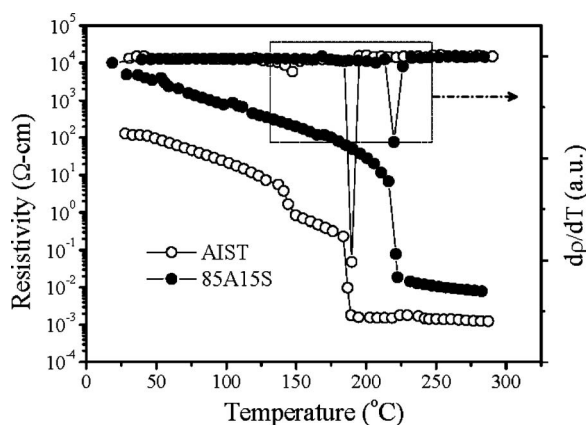
Figure 2. Typical ρ and corresponding *d*ρ/*dT* profiles as a function of temperature for 150nm thick AIST and 85A15S layers measured at the heating rate of 1°C/min.

quentially deposited on by sputtering and followed by a liftoff process to from desired device pattern. The cross-sectional view of PCM device is schematically shown in Fig. 1. Static *I–V* characteristics were measured by an HP4156B semiconductor parameter analyzer (Agilent Technologies) at dc mode.

Results and Discussion

Figure 2 shows the typical ρ and corresponding derivatives (*d*ρ/*dT*) profiles for 150-nm-thick AIST and 85A15S layers as a function of temperature measured at a heating rate of 1°C/min. It can be seen that the ρ profile shifts upward when SiO_2 is added in AIST. The escalation of sample resistance should result from the incorporation of high-resistive SiO_2 phase, emergence of chalcogenide/SiO_2 interfaces, and the refinement of AIST grains, as revealed by subsequent microstructure analyses. Figure 2 also shows that the incorporation of SiO_2 in 85A15S nanocomposite does not alter the differences of ρ in between amorphous and crystalline states such that the resistance ratios remain similar at about 10^4 times for pristine and nanocomposite samples. In particular, Fig. 2 depicts a mild drop prior to the obvious drop in ρ profile for the pristine AIST, indicating that its phase transition seems to proceed in a two-step manner. Such a phenomenon was observed in all pristine AIST samples prepared in this work regardless of their thicknesses, and its correlation to possible microstructure change will be discussed later. It is also noted that this phenomenon is missed in previous studies regarding Sb_2Te alloys and its nanocomposites using either optical[20] or calorimetry methods.[21,22] This illustrates that electrical property measurement is a valuable tool with better sensitivity for characterizing the phase-change behaviors of thin-film chalcogenide samples. Further, according to the *d*ρ/*dT* profiles shown in Fig. 2, the values of T_x are determined as 187 and 222°C for the pristine AIST and 85A15S samples, respectively. The increment of T_x has been attributed to the restriction of surface atomic motion on AIST nanocrystals caused by coherent bonding with the surrounding atoms at the interface.[23,24] Nevertheless, from a structure point of view, the dispersed SiO_2 particles form structure discontinuities in AIST, which impede the growth and coalescence of AIST during recrystallization. The retardation increases the thermal resistance of nanocomposite sample due to the generation of numer-
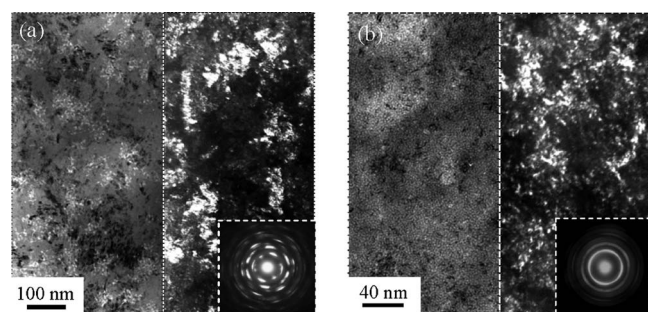

Figure 3. In situ heating XRD patterns of (a) AIST and (b) 85A15S. (c) Integrated values and fwhms of (103) peaks for the AIST and 85A15S layers.

Figure 4. PTEM micrographs of (a) AIST and (b) 85A15S samples subjected to annealing at 250°C for 1 h. The left-hand part is the bright field (BF) image while the right-hand part is the dark field (DF) image. Corresponding SAED pattern is inserted at the right-hand corner of each micrograph.

Table I. A list of T_x and E_a for AIST and 85A15S samples calculated in terms of Kissinger's theory.

| Sample thickness (nm)	AIST		85A15S	
	T_x (°C)[a]	E_a (eV)[b]	T_x (°C)[a]	E_a (eV)[b]
30	199	2.5	253	3.2
50	195	2.2	237	2.5
100	195	2.1	234	2.3
150	193	2.1	226	2.3

[a] Representative T_x's were measured at heating rate = 5°C/min.
[b] Kissinger's analysis was performed at various heating rates = 1, 2.5, 5, 7.5, 10 and 12.5°C/min for the determination of E_a.

ous interfacial defects inside, implying the superheat effect that causes the rise of T_x and hence the stabilization of amorphous AIST. This argument is further supported by the Kissinger's analysis and microstructure characterizations presented as follows.

In situ heating XRD was carried out in order to clarify the structure changes and the ambiguities observed in ρ profiles. Figures 3a and b separately present the XRD spectra for AIST and 85A15S obtained at different temperatures. It can be seen that in both samples AIST transforms from initially amorphous structure to hexagonal crystal structure (PDF #801722) structure during heating. Specific attention was paid to the temperature range corresponding to the mild drops in ρ profiles during XRD experiment; however, the diffraction patterns remained fuzzy, broad profiles without the presence of characteristic peaks. This implied the absence of transition or intermediate phase during the amorphous-to–crystalline transition. Crystalline defects such as vacancies and interstitial atoms are known to be effective scattering centers of charge carriers; the mild drop in ρ profile is hence attributed to the structure recovery in AIST which eliminates these point defects prior to the occurrence of recrystallization.[25] Further, it is believed that subgrains should have emerged in AIST at the temperature when the mild drop in ρ occurs (i.e., about 150°C). Rearrangement and/or annihilation of linear and planar defects, e.g., dislocations and grain boundaries, may also contribute the decrement of ρ in the sample.[25,26] As to 85A15S sample, the JMA analysis presented below indicates that its phase transition likely proceeds in heterogeneous manner. This promotes the steady-state nucleation rate and hence smears out the mild drop appearing in ρ profile for 85A15S sample.

Figure 3c presents the integrated intensities and corresponding full-width-half-maximum (fwhm) of (103) XRD peaks as a function of temperature for AIST and 85A15S layers. Derivatives of integrated intensity profiles with respect to temperature delineate the onsets of recrystallization for AIST and 85A15S at around 189 and 223°C, respectively. Disregarding the temperature detection errors, there is good agreement with the results deduced by electrical property measurement. Further, Fig. 3c depicts that nanocomposite sample possesses a larger fwhm of characteristic XRD peak, implying that the incorporation of SiO$_2$ causes the AIST grain refinement. This is further confirmed by TEM characterization presented below.

Figures 4a and b, respectively, present the plan-view transmission electron microscopy (PTEM) micrographs and corresponding selected area electron diffraction (SAED) patterns (attached at the lower right-hand corners of TEM micrographs) for AIST and 85A15S samples subjected to an annealing treatment at 250°C for 1 h. Polycrystalline grain structure and a reduction of AIST grain size due to the SiO$_2$ addition in nanocomposite sample can be readily seen from the structure evolution depicted by Fig. 4a and b. Further, the indexing of SAED patterns indicates that both samples possess the hexagonal crystal structure, confirming the results of

XRD analysis presented above. The attached SAED patterns also reveal a texturelike structure in the pristine AIST, and the dispersed SiO$_2$ indeed randomizes the spatial orientation of AIST grains in 85A15S sample.

Table I summarizes the representative values of T_x obtained by electrical measurement and E_a calculated from the Kissinger plots (i.e., the plots of $\ln(\varphi/T_x^2)$ vs $1/T$, where φ = the heating rate)[17] for pristine AIST and 85A15S layers at various sample thicknesses. As shown in Table I, the values of T_x and E_a for both samples increase with the decrease of film thickness. This is mainly ascribed to the restraint of sample dimension on the progress of grain growth during recrystallization.[19] Further, heat propagation in the sample becomes difficult when the film thickness decreases; restriction on energy supply might also cause the delay of phase transition. As to the samples at the same thickness, the addition of SiO$_2$ in nanocomposite increases the values of T_x and E_a. Arguments relating to the chemical reactivity,[24] degree of nucleation,[27,28] and stress status at the chalcogenide/SiO$_x$ interface[29] have been proposed to explain the increase of E_a. From a structure point of view, hindrance to grain growth during recrystallization due to the incorporation of SiO$_2$ is the main cause for the increase of T_x and E_a in the nanocomposite. Further, as revealed by electrical measurements, increase of thermal resistance in 85A15S sample may also affect the values of T_x and E_a. Refinement of AIST grains and dispersed SiO$_2$ particles in sample matrix are known to interrupt the lattice periodicity. The lattice discontinuities, e.g., grain boundaries in AIST as well as the newly formed AIST/SiO$_x$ interfaces, would retard phonon propagation and thus degrade thermal conduction in the nanocomposite. Figure 2 depicts an overall increase of ρ in 85A15S sample, indicating that the incorporation of SiO$_2$ upsets charge carrier transport in nanocomposite regardless of the crystallinity of AIST. Electronic contribution to thermal conduction in elemental semiconductors is negligibly small due to the low carrier concentrations (e.g., about 10^{10} cm^{-3} for Si).[30] However, SbTe-series chalcogenides are known to be p-type semiconductors with comparatively high carrier concentrations (10^{19}–10^{25} cm^{-3}),[31,32] so that the electronic contribution to thermal conduction should not be ruled out. In other words, suppression of thermal conduction in the nanocomposite can also be inferred from the increment of ρ, as revealed by Fig. 2. As a result, the 85A15S sample would experience a higher thermal resistance and consequently discourage the heat propagation. This results in a delay of phase transition and hence an increase of T_x and E_a occurs in the nanocomposite sample.

For JMA analysis, the data obtained by isothermally soaking the samples at various temperatures below T_x were first transformed to the crystallization fraction $x(t)$ according to the expression $x(t) = (\rho_\alpha - \rho(t))/(\rho_\alpha - \rho_c)$, where ρ_α and ρ_c denote the values of ρ for completely amorphous and crystalline films observed during the experiment, respectively. The S-shaped $x(t)$ vs t profiles for the pristine AIST and 85A15S samples are shown in Fig. 5a and b, respectively, and they can be related to the JMA equation, $x(t) = 1 - \exp(-\kappa t^n)$, where n is the Avrami exponent and κ is an effective
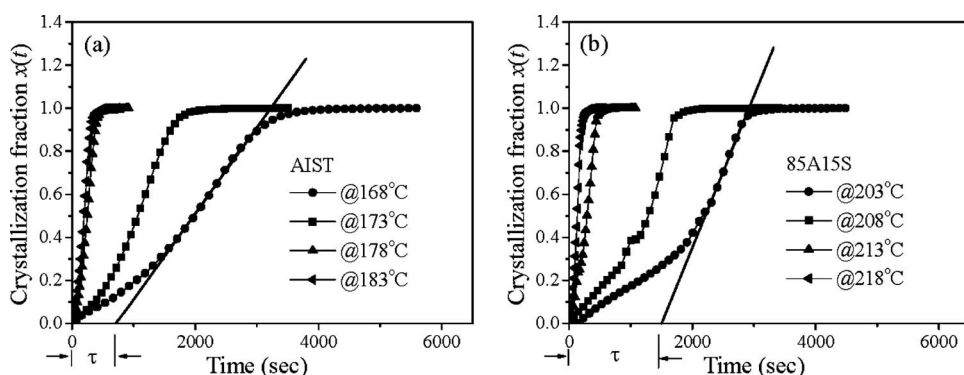
Figure 5. Plots of crystallization fraction $x(t)$ vs t obtained at various temperatures below T_x of (a) pristine AIST and (b) 85A15S samples.

rate constant. By analyzing the slope of $\ln\{-\ln[1 - x(t)]\}$ vs $\ln t$ plot (i.e., the JMA plot), the value of n can be determined. We note that when performing JMA analysis, the starting point of phase transition has to be determined in a manner consistent with the phase transition principles in order to secure reasonable values of n.[18,19,33] Classical theory of nucleation and growth divides the phase transition into four stages, i.e., incubation period, steady-state nucleation, growth, and coarsening.[19,26] At incubation period, phase transition is time-dependent which violates one of the assumptions of JMA theory, and hence this part of data has to be expelled from JMA analysis. To fulfill this requirement, extrapolation of $x(t)$ was first performed to determine the incubation time span (τ), as illustrated in Fig. 5. The starting point of phase transition was then defined at $t = \tau$, and the data obtained at $t > \tau$ were extracted for JMA analysis. A careful examination of Fig. 5a and b found that the value of τ for the 85A15S sample is comparatively larger than that for the pristine AIST at the same testing condition, indicating that the SiO_2 addition in the nanocomposite sample indeed delays the phase transition due to the suppression of thermal conduction.[9,34] Further, in steady-state nucleation regime, the extrapolating line for determining the value of τ was found to exhibit a steeper slope in the case of 85A15S sample, as shown in Fig. 5b. This indicates that although the crystalline AIST embryos take more time to become stable nuclei in incubation period due to the restriction on heat transfer, the number of stable AIST crystallites in the 85A15S sample increases in a faster rate once the phase transition proceeds to the steady-state nucleation stage. This is ascribed to the embedded SiO_2 particles which provide numerous sites for the formation of crystalline AIST phase in the 85A15S sample. This supports the heterogeneous concept of phase transition[19,26] that would accelerate the steady-state nucleation rate of AIST in 85A15S sample during recrystallization, as illustrated in Fig. 5b.

Table II lists the values of n calculated in terms of the data handling method described above. According to JMA theory, n can be correlated to the progress mode of phase transition, e.g., $2 \leqslant n \leqslant 3$ implies the two-dimensional mode, while $3 \leqslant n \leqslant 4$ implies the three-dimensional mode. It can be seen that the value of n decreases with the decrease of film thickness for both sample types,

iterating the sample dimension effects on phase transition. The reduction of film thickness limits the spatial freedoms when new phase advances in the sample. Hence, the phase transition switches from the three-dimensional mode in thick sample to the two-dimensional mode in thin sample. Further, as shown in Table II, at the same sample thickness the nanocomposite sample possesses the lower value of n. Decrease of n's is in agreement with the results reported previously[16,35] that the dispersed SiO_2 particles provide additional nucleation sites and thus promote the heterogeneous phase transition[19,26] in nanocomposite sample. It is believed that the chalcogenide/SiO_x interfaces may serve as the preferential sites igniting the nucleation, and recrystallization is expected to proceed in two-dimensional manner since grain boundaries are well-known planar defects.[26] The dispersed SiO_2 further imposes spatial constraint on growth path, which would limit the progress of phase transition in lower dimensional modes. Finally, some phase transition textbooks list definite phase transition mechanisms in terms of the values of n.[19] We however decline a proposal on detailed mechanism due to the lack of direct microstructure evidence as well as the presence of uncertainties, such as nonuniform seeding,[36] finite size effects,[36,37] surface, and interface crystallization[38] in the samples, which will also affect the phase transition process.

Table II also lists the values of ΔH calculated in terms of the knowledge of κ (i.e., the intercepts of JMA plots at $\ln t \rightarrow 0$) in conjunction with the expression $\kappa = \kappa_0 \exp(-\Delta H / k_B T)$ in which k_B = Boltzmann's constant. It has been showed that ΔH is correlated to n by the equation $\Delta H = E_n + (n - 1)E_g$, in which E_n = activation energy for nucleation process and E_g = activation energy for growth process.[39] In the same sample type, the increase of ΔH with the increase of sample thickness is mainly ascribed to the increase of n or the increase of dimensionality of phase transition mode in thick samples. At the same sample thickness, the 85A15S exhibits a higher value of ΔH in comparison with the pristine AIST. Since heterogeneous phase transition in 85A15S mainly contributes to the decrease of E_n, hence the increase of ΔH is resulted from the dramatic increase of E_g due to the growth barrier effect of SiO_2 in nancomposite sample.

Figure 6a presents the static I–V characteristics of PCM devices containing pristine AIST and 85A15S programming layers. The presence of switching threshold behavior illustrates that these chalcogenide layers are indeed feasible to PCM fabrication. Further, it can be seen that the switching voltage (V_{th}) of device containing 85A15S layer (V_{th} = 1.65 V) is higher than that of the device containing pristine AIST (V_{th} = 1.10 V). We note that the occurrence of V_{th} indicates the onset of amorphous-to-crystalline transition in programming layer of PCM devices. The high V_{th} for 85A15S sample can thus be ascribed to the incorporation of SiO_2 which hinders the growth of AIST crystallites during the recrystallization of amorphous AIST in nanocomposite. This also means nanocomposite containing amorphous AIST is able to sustain a higher electromotive force when serving as the programming layer of PCM devices. This

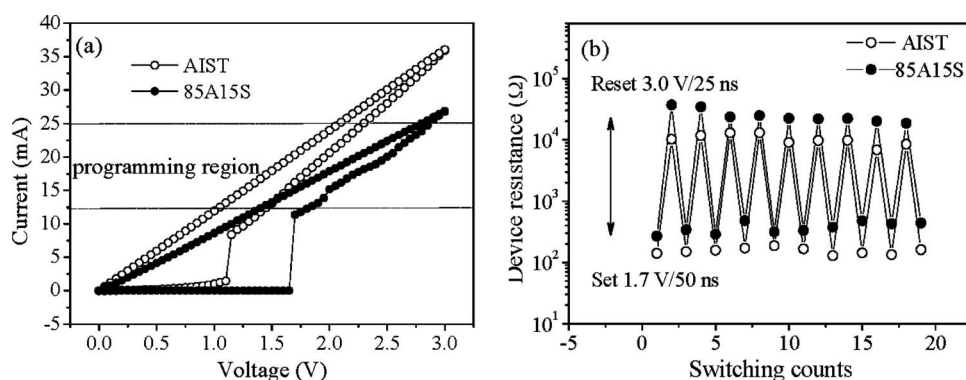**Table II. A list of n and ΔH for AIST and 85A15S samples calculated in terms of JMA theory.**

Sample thickness (nm)	AIST		85A15S	
	n^a	ΔH (eV)	n^a	ΔH (eV)
30	2.9	3.7	2.5	3.9
50	2.9	4.4	2.6	4.8
100	3.2	4.5	2.8	5.2
150	3.3	4.9	2.9	5.3

^{a} We added 1 to the values of n to compensate the dimension effect since the data were acquired from thin-film samples.[19]

Figure 6. (a) Static *I–V* profiles and (b) binary switching behaviors for PCM devices containing AIST or 85A15S as the programming layers.

illustrates that utilization of nanocomposite would benefit the thermal stability of the programming layer in amorphous state.

Dynamic resistance is defined as the resistance measured in the programming region. According to Fig. 6a, the dynamic resistances of the device corresponding to the pristine AIST and 85A15S layers are found to be about 80 and 120 Ω, respectively. Increase of dynamic resistance may thus lead to the reduction of writing current. This is in agreement with previous studies on GST–SiO$_x$ PCM (Ref. 9 and 34), and a reduction of power consumption can be expected in the PCM containing chalcogenide nanocomposite as the programming layers. Though the SiO$_2$ incorporation for the improvement of PCM device performance has been demonstrated,[9,34] the influences of interface geometry on the thermal conduction of nanocomposite layers and relating PCM device properties are not quantitatively discussed. Since interfaces are considered as the carrier scattering centers, it is reasonable to infer that the thermal conductivity of the nanocomposite layer can be manipulated by varying the amount and morphology of chalcogenide–SiO$_2$ interfaces. This would lead to a device performance modification of PCMs containing nanocomposites as the programming layers and thus a better understanding on the relevance of microstructure change and physical properties.

Figure 6b depicts a typical reversible binary switching behavior between lower resistance (LR) and high resistance (HR) states. The presence of HR and LR levels for binary switching of 85A15S samples implies that the addition of SiO$_2$ does not degrade the phase-change reversibility of AIST, and the result iterates the feasibility of AIST nanocomposite layers for PCM applications.

Conclusions

The phase transition kinetics and microstructure changes of the AIST and its nanocomposite layers were investigated. In situ electrical property measurement found that the incorporation of SiO$_2$ increases both the levels of ρ for amorphous and crystalline states of nanocomposite sample; however, it does not alter the difference in ρ which remains at about 10^4 times. In situ heating XRD analysis revealed that the structure transition of all samples proceeds in a one-step, amorphous-to-crystalline manner. Electrical property measurement in conjunction with XRD and TEM characterizations also illustrated that the SiO$_2$ embedment is able to stabilize the amorphous state of sample and causes the grain refinement in AIST during recrystallization.

Kissinger analysis showed that SiO$_2$ addition causes the increase of T_x and E_a for the nanocomposite layer, implying the retardation of grain growth in AIST in such a sample. From a structure point of view, incorporation of SiO$_2$ is the main cause for the increase of T_x and E_a. Further, refinement of AIST grains and the emergence of numerous chalcogenide/SiO$_x$ interfaces escalate the thermal resistance of nanocomposite sample. Restriction of heat supply hence delays the phase transition in nanocomposite and causes the rise of T_x and E_a. Isothermal experiment in conjunction with JMA analysis revealed that the formation of nanocomposite results in the decrease of Avrami exponent (n), indicating that the recrystallization of AIST

in nanocomposite is prone to heterogeneous manner. Calculation of appropriate activation energy (ΔH) implied a dramatic increase of activation energy for growth process, evidencing that the dispersed SiO$_2$ indeed serves as the obstacles of grain growth during recrystallization.

The static *I–V* characteristics of PCM devices containing various programming layers illustrated not only the feasibility of these chalcogenide layers to PCM fabrication but also the escalation of the switching V_{th} from 1.10 V for the AIST device to 1.65 V for the 85A15S device. Incorporation of SiO$_2$ caused the increase of dynamic resistance and hence the reduction of programming current, which would benefit the power efficiency for device operation. Binary switching test showed no degradation on phase-change reversibility of AIST in the nanocomposite layer.

References

1. Y. Yin, H. Sone, and S. Hosaka, *J. Appl. Phys.*, **102**, 064503 (2007).
2. Y. F. Lai, B. W. Qiao, J. Feng, Y. L. Ling, L. Z. Lai, Y. Y. Lin, T. A. Tang, B. C. Cai, and B. Chen, *J. Electron. Mater.*, **34**, 176 (2005).
3. L. Men, J. Tominaga, H. Fuji, and N. Atoda, *Jpn. J. Appl. Phys.*, **39**, 2639 (2000).
4. N. Matsuzaki, K. Kurotsuchi, Y. Matsui, O. Tonomura, N. Yamamoto, Y. Fujisaki, N. Kitai, R. Takemura, K. Osada, S. Hanzawa, et al., *Tech. Dig. - Int. Electron Devices Meet.*, 2005, 758
5. J. Feng, Z. F. Zhang, Y. Zhang, B. C. Cai, Y. Y. Lin, T. A. Tang, B. C. Cai, and B. Chen, *J. Appl. Phys.*, **101**, 074502 (2007).
6. T. Zhang, Z. Song, F. Rao, G. Feng, B. Liu, S. Feng, and B. Chen, *Jpn. J. Appl. Phys., Part 2*, **46**, L247 (2007).
7. T. Y. Lee, S. S. Yim, D. Lee, M. H. Lee, D. H. Ahn, and K. B. Kim, *Appl. Phys. Lett.*, **101**, 074502 (2007).
8. S. Privitera, E. Rimini, and R. Zonca, *Appl. Phys. Lett.*, **85**, 3044 (2004).
9. S. W. Ryu, J. H. Oh, B. J. Choi, S. Y. Hwang, S. K. Hong, C. S. Hwang, and H. J. Kim, *Electrochem. Solid-State Lett.*, **9**, G259 (2006).
10. L. van Pieterson, M. H. R. Lankhorst, M. van Schijndel, A. E. T. Kuiper, and J. H. J. Roosen, *J. Appl. Phys.*, **97**, 083520 (2005).
11. B. J. Kooi and J. Th. M. De Hosson, *J. Appl. Phys.*, **95**, 4714 (2004).
12. T. Ohta, in *Joint International Symposium on Optical Memory and Optical Data Storage* SPIE, p. 188, Kauai, HI (1999).
13. N. Yamada, T. Matsunaga, in E*PCOS 2003, European Symposium on Phase Change and Ovonic Science* p. 7, Lake Lugano, Switzerland (2003).
14. M. Shinotsuka, N. Onagi, and M. Harigaya, *Jpn. J. Appl. Phys., Part 1*, **39**, 976 (2000).
15. H. C. Mai and T. E. Hsieh, *Jpn. J. Appl. Phys., Part 1*, **46**, 5834 (2007); H. C. Mai and T. E. Hsieh, *Jpn. J. Appl. Phys., Part 1*, **47**, 6029 (2008).
16. Y.-J. Huang, Y.-C. Chen, and T.-E. Hsieh, *J. Appl. Phys.*, **106**, 034916 (2009).
17. H. E. Kissinger, *Anal. Chem.*, **29**, 1702 (1957).
18. M. Avrami, *J. Chem. Phys.*, **7**, 1103 (1939); M. Avrami, *J. Chem. Phys.*, **8**, 212

(1940); M. Avrami, *J. Chem. Phys.*, **9**, 177 (1941).

19. J. W. Christian, *The Theory of Transformations in Metals and Alloys, Part I, Equilibrium and General Kinetic Theory*, 2nd ed., pp. 15, 525, Pergamon, Oxford (1975).
20. G. Mongia and P. Bhatnagar, *J. Mater. Sci.*, **41**, 2477 (2006).
21. J. Kalb, F. Spaepen, and M. Wuttig, *J. Appl. Phys.*, **93**, 2389 (2003).
22. R. Detemple, H. Dieker, J. Kalb, M. Luo, F. Spaepen, C. Steimer, D. Wamwangi, H. W. Wöltgens, M. Wuttig and S. Ziegler, in *E\PCOS 2004, European Symposium on Phase Change and Ovonic Science*, p. 4, Balzers, Liechtenstein (2004).
23. N. Ohshima, *J. Appl. Phys.*, **79**, 8357 (1996); N. Ohshima, *J. Appl. Phys.*, **83**, 5244 (1998).
24. Q. Jiang, H. Tong, D. Hsu, K. Okuyama, and F. Shi, *Thin Solid Films*, **312**, 357 (1998).
25. J. D. Verhoeven, *Fundamentals of Physical Metallurgy*, p. 331, John Wiley & Sons, New York (1975).
26. R. E. Reed-Hill and R. Abbaschian, *Physical Metallurgy Principles*, 3rd ed., PWS, Boston (1992).
27. M. Zacharias, J. Blasing, and P. Veit, *Appl. Phys. Lett.*, **74**, 2614 (1999).
28. M. Zacharias and P. Streitenberger, *Phys. Rev. B*, **62**, 8391 (2000).
29. J. Tominaga, T. Nakano, and N. Atoda, *Jpn. J. Appl. Phys., Part 1*, **37**, 1852 (1998).

30. S. M. Sze, *Semiconductor Devices, Physics and Technology*, 2nd ed. p. 538, John Wiley & Sons, New York (2002).
31. B. Huang, C. Lawrence, A. Gross, G.-S. Hwang, N. Ghafouri, S.-W. Lee, H. Kim, C.-P. Li, C. Uher, K. Najafi, et al., *J. Appl. Phys.*, **104**, 113710 (2008).
32. H. Zou, D. M. Rowe, and G. Min, *J. Vac. Sci. Technol. A*, **19**, 899 (2001).
33. V. Weidenhof, I. Friedrich, S. Ziegler, and M. Wuttig, *J. Appl. Phys.*, **89**, 3168 (2001).
34. T.-Y. Lee, K. H. P. Kim, D.-S. Suh, C. Kim, Y.-S. Kang, D. G. Cahill, D. Lee, Min-Hyun Lee, M.-H. Kwon, K.-B. Kim, et al., *Appl. Phys. Lett.*, **94**, 243103 (2009).
35. C. R. Rodríguez, E. Prokhorov, G. Trapaga, E. M. Sánchez, M. H. Landaverde, Yu. Kovalenko, and J. G. Hernández, *J. Appl. Phys.*, **96**, 1040 (2004).
36. V. Sessa, M. Fanfoni, and M. Tomelini, *Phys. Rev. B*, **91**, 007146 (1989).
37. M. C. Weinberg, *J. Non-Cryst. Solids*, **134**, 116 (1991); M. C. Weinberg, *J. Non-Cryst. Solids*, **142**, 126 (1992); M. C. Weinberg, *J. Non-Cryst. Solids*, **219**, 89 (1997), M. C. Weinberg, *J. Chem. Phys.*, **91**, 7146 (1989).
38. T. H. Jeong, M. R. Kim, H. Seo, S. J. Kim, and S. Y. Kim, *J. Appl. Phys.*, **86**, 774 (1999).
39. G. Ruitenberg, A. K. Petford-Long, and R. C. Doole, *J. Appl. Phys.*, **92**, 3116 (2002).